Heterometal Cuboidal Clusters $MFe_4S_6(PEt_3)_4Cl$ (M = V, Mo): Synthesis, Structural Analysis by Crystallography and EXAFS, and Relevance to the Core Structure of the Iron–Molybdenum Cofactor of Nitrogenase

E. Nordlander,[1a,b] Sonny C. Lee,[1a] Wei Cen,[1a] Z. Y. Wu,[1c] C. R. Natoli,[1c] A. Di Cicco,[1d] A. Filipponi,[1e] Britt Hedman,[1f] Keith O. Hodgson,*[,1f,g] and R. H. Holm,*[,1a]

Contribution from the Department of Chemistry, Harvard University, Cambridge, Massachusetts 02138, INFN, Laboratori Nazionali di Frascati, C.P. 13, 00044, Frascati, Italy, Dipartimento di Matematica e Fisica, Università degli Studi di Camerino, Via Madonna delle Carceri, 63032 Camerino, Italy, Dipartimento di Fisica, Università degli Studi dell'Aquila, Via Vetoio, 67010 Coppito-L'Aquila, Italy, and Department of Chemistry and Stanford Synchrotron Radiation Laboratory, Stanford University, Stanford, California 94305

Received January 4, 1993

Abstract: The cluster self-assembly system $MCl_3(THF)_3/2FeCl_2(PEt_3)_2/4–7(Me_3Si)_2S$ affords, after separation of cluster coproducts, the isomorphous compounds $MFe_4S_6(PEt_3)_4Cl$ (M = V, Mo) in modest yields. These species were identified by spectroscopic methods and X-ray diffraction. The compounds crystallize in trigonal space group $R\bar{3}c$; the cluster molecules are isostructural and essentially isometric. They consist of a cuboidal Fe_4S_3 fragment that is bridged by three μ_2-S atoms to a M–PEt_3 unit whose M–P bond is coincident with an imposed C_3 axis. Coordination is completed at the three symmetry-related Fe sites by PEt_3 ligands and at the Fe site on the C_3 axis by chloride. The trigonal pyramidal coordination units FeS_3P and MoS_3P are infrequently observed and unprecedented, respectively, and the cuboidal fragment has been observed previously only in several Fe–S–nitrosyl clusters. The cluster structure presents atoms at a series of distances from the M or Fe atoms and has been utilized in a detailed test of distance determinations in a new approach to the analysis of EXAFS data using theoretical phases and amplitudes (the GNXAS approach). The Mo and Fe EXAFS of the cluster $MoFe_4S_6(PEt_3)_4Cl$ have been analyzed in detail and first coordination shell distances determined with high accuracy. The contribution of multiple scattering pathways in the EXAFS of the cluster has been evaluated. The relevance of the results to the FeMo-cofactor structure as recently deduced from protein crystallography is considered.

Introduction

Continuing developments emphasize the significance of cuboidal and cubane-type structures of metal–sulfur clusters in biology. For example, the most recently characterized iron–sulfur cluster type has the Fe_3S_4 cuboidal structure **1**[2-4] in Figure 1. This protein-bound unit may be reconstituted with Fe^{2+} to yield the pervasive Fe_4S_4 cubane-type cluster **2** or with other exogenous metal ions to afford the heterometal MFe_3S_4 cubane-type clusters **3**.[5] As indicated (Figure 1), certain of these clusters[6-8] and others, including those of vanadium[9] and molybdenum,[10-12] can also be synthesized by the methods of self-assembly and fragment condensation.[12] The cubane-type structure of protein-bound MFe_3S_4 clusters with M = Co and Ni has been demonstrated by the near-identity of their spectroscopic properties with those of synthetic clusters of known structures.[8,13]

Heterometal cubane clusters with M = Mo (**4**) and V (**5**) are the best available models of the *local* environments of these atoms in the cofactors of nitrogenase, on the basis of X-ray absorption spectroscopic (edge and extended X-ray fine structure (EXAFS)) criteria.[14,15] Thus, in Figure 1 the bolded cuboidal MFe_3S_3 portions of these clusters conform to the results obtained from analysis of the molybdenum and vanadium EXAFS of nitrogenase

(1) (a) Harvard University. (b) Swedish Natural Science Research Foundation Postdoctoral Fellow, 1990–1992. (c) INFN. (d) Università degli Studi di Camerino. (e) Università degli Studi dell'Aquila. (f) Stanford Synchrotron Radiation Laboratory. (g) Stanford University.

(2) (a) Stout, C. D. *J. Biol. Chem.* **1988**, *263*, 9256; *J. Mol. Biol.* **1989**, *205*, 545. (b) Martin, A. E.; Burgess, B. K.; Stout, C. D.; Cash, V. L.; Dean, D. R.; Jensen, G. M.; Stephens, P. J. *Proc. Natl. Acad. Sci. U.S.A.* **1990**, *87*, 598. (c) Soman, J.; Iismaa, S.; Stout, C. D. *J. Biol. Chem.* **1991**, *266*, 21558.

(3) Robbins, A. H.; Stout, C. D. *Proteins: Struct., Func., Genet.* **1989**, *5*, 289.

(4) (a) Kissinger, C. R.; Adman, E. T.; Sieker, L. C.; Jensen, L. H. *J. Am. Chem. Soc.* **1988**, *110*, 8721. (b) Kissinger, C. R.; Sieker, L. C.; Adman, E. T.; Jensen, L. H. *J. Mol. Biol.* **1991**, *219*, 693.

(5) (a) Moura, I.; Moura, J. J. G.; Münck, E.; Papefthymiou, V.; LeGall, J. J. *J. Am. Chem. Soc.* **1986**, *108*, 348. (b) Surerus, K. K.; Münck, E.; Moura, I.; Moura, J. J. G.; LeGall, J. *J. Am. Chem. Soc.* **1987**, *109*, 3805. (c) Conover, R. C.; Park, J.-B.; Adams, M. W. W.; Johnson, M. K. *J. Am. Chem. Soc.* **1990**, *112*, 4562. (d) Butt, J. N.; Armstrong, F. A.; Breton, J.; George, S. J.; Thomson, A. J.; Hatchikian, E. C. *J. Am. Chem. Soc.* **1991**, *113*, 6663. (e) Butt, J. N.; Sucheta, A.; Armstrong, F. A.; Breton, J.; Thomson, A. J.; Hatchikian, E. C. *J. Am. Chem. Soc.* **1991**, *113*, 8948. (f) Thomson, A. J.; Breton, J.; Butt, J. N.; Hatchikian, E. C.; Armstrong, F. A. *J. Inorg. Biochem.* **1992**, *47*, 197.

(6) Roth, E. K. H.; Greneche, J. M.; Jordanov, J. *J. Chem. Soc., Chem. Commun.* **1991**, 105.

(7) (a) Ciurli, S.; Yu, S.-B.; Holm, R. H.; Srivastava, K. K. P.; Münck, E. *J. Am. Chem. Soc.* **1990**, *112*, 8169. (b) Ciurli, S.; Ross, P. K.; Scott, M. J.; Yu, S.-B.; Holm, R. H. *J. Am. Chem. Soc.* **1992**, *115*, 5415.

(8) Zhou, J.; Scott, M. J.; Hu, Z.; Peng, G.; Münck, E.; Holm, R. H. *J. Am. Chem. Soc.* **1992**, *114*, 10843.

(9) (a) Kovacs, J. A.; Holm, R. H. *Inorg. Chem.* **1987**, *26*, 702, 711. (b) Ciurli, S.; Holm, R. H. *Inorg. Chem.* **1989**, *28*, 1685.

(10) Holm, R. H.; Simhon, E. D. In *Molybdenum Enzymes*; Spiro, T. G., Ed.; Wiley-Interscience: New York, 1985, Chapter 1.

(11) Coucouvanis, D.; Al-Ahmad, S. A.; Salifoglou, A.; Papaefthymiou, V.; Kostikas, A.; Simopoulos, A. *J. Am. Chem. Soc.* **1992**, *114*, 2472.

(12) Holm, R. H. *Adv. Inorg. Chem.* **1992**, *38*, 1. This article provides a comprehensive account of MFe_3S_4 clusters.

(13) Srivastava, K. K. P.; Surerus, K. K.; Conover, R. C.; Johnson, M. K.; Park, J.-B.; Adams, M. W. W.; Münck, E. *Inorg. Chem.* **1993**, *32*, 927.

(14) Mo K-edge EXAFS: (a) Cramer, S. P.; Hodgson, K. O.; Gillum, W. O.; Mortenson, L. E. *J. Am. Chem. Soc.* **1978**, *100*, 3398. (b) Conradson, S. D.; Burgess, B. K.; Newton, W. E.; Mortenson, L. E.; Hodgson, K. O. *J. Am. Chem. Soc.* **1987**, *109*, 7507.

(15) V K-edge EXAFS: (a) Arber, J. M.; Dobson, B. R.; Eady, R. R.; Stevens, P.; Hasnain, S. S.; Garner, C. D.; Smith, B. E. *Nature (London)* **1987**, *325*, 327. (b) George, G. N.; Coyle, C. L.; Hales, B. J.; Cramer, S. P. *J. Am. Chem. Soc.* **1987**, *109*, 6854. (c) Arber, J. M.; Dobson, B. R.; Eady, R. R.; Hasnain, S. S.; Garner, C. D.; Matsushita, T.; Nomura, M.; Smith, B. E. *Biochem. J.* **1989**, *258*, 733.

0002-7863/93/1515-5549$04.00/0

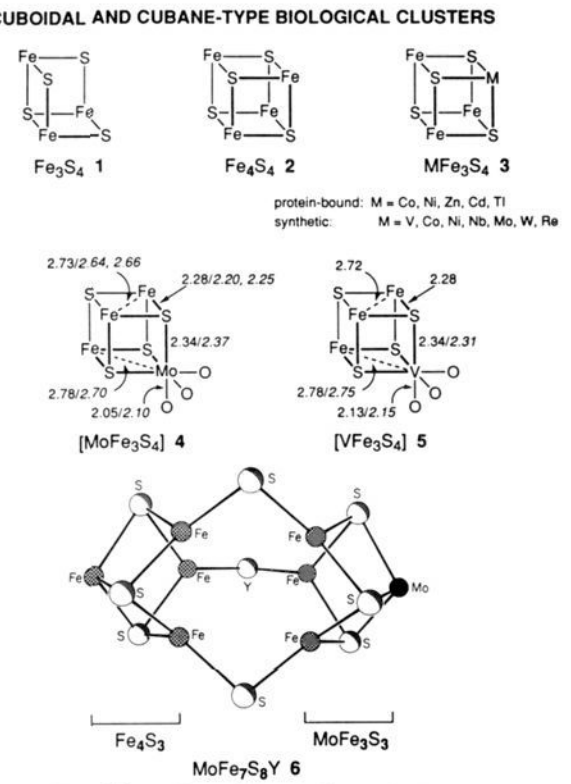

Figure 1. Top: Illustrations of the cuboidal Fe_3S_4 (**1**) and cubane-type Fe_4S_4 (**2**) and MFe_3S_4 (**3**) cores of protein-bound and synthetic (**2**, **3**) clusters. Center: Comparison of typical bond distances in the synthetic clusters $MoFe_3S_4$ (**4**) and VFe_3S_4 (**5**) from X-ray diffraction with those determined from Mo, V, and Fe EXAFS analysis (italics) of the FeMo/V proteins of nitrogenase and the FeMo-cofactor. The bolded portions are common to the synthetic and native clusters. Bottom: Representation of the KR FeMo-cofactor structure model (**6**).[20]

proteins and cofactors. The synthesis of clusters containing **4** and **5**, which in their normally accessible oxidation states are anionic, has been performed in polar media such as methanol or acetonitrile. Under conditions of self-assembly in such solvents, we have not been successful in obtaining clusters with the 6–8:1 Fe:Mo atom ratio indicated by chemical analysis of the FeMo-cofactor.[16] Indeed, only cubane clusters have been realized under these conditions. However, we have shown that certain uncharged iron–sulfur clusters with noncubane structures can be prepared by self-assembly in THF solutions. These include the hexanuclear "basket" clusters $Fe_6S_6(PR_3)_4X_2$ (X = halide, RS^-)[17,18] and heptanuclear $Fe_7S_6(PEt_3)_4Cl_3$,[19] having the idealized monocapped prismane core. These results show that higher nuclearity structures can be assembled in a solvent of low polarity and suggest that new *hetero*metal clusters may be accessible by related reactions in such media.

With the structural model **6** (Figure 1) deduced from X-ray diffraction data of the FeMo-protein of *Azotobacter vinelandii* now available from the highly significant work of Kim and Rees,[20] the importance of the cuboidal stereochemistry in native clusters is accentuated. In this structure (hereafter, the KR model), there are two cuboidal fragments, Fe_4S_3 and $MoFe_3S_3$. These are linked by two sulfide bridges and an unidentified atom Y.

While EXAFS analysis has contributed significant insights to the structural nature of the heterometal cuboidal units in FeMo-proteins and the FeMo-cofactor,[14-16,21-23] and for synthetic MFe_3S_4 cubane-type clusters, the approaches have not been without their limitations. For analysis approaches based on empirical amplitudes and phases,[24] there is sometimes difficulty in obtaining suitable models for extraction of reliable parameters. For example, this situation led to an initial ambiguity in distinguishing by EXAFS between two possible structural models for the Mo site of the FeMo protein.[14a] The empirical approach is of questionable utility for atoms beyond *ca.* 3 Å from the absorber. This is in part because of the limited possibility of obtaining reliable empirical phase and amplitude parameters and in part because of the limitation that multiple scattering (MS) effects cannot (where significant) be analyzed properly and thus distinguished from single scattering pathways at similar distances.[25] Recent improvements in the derivation and application of accurate theoretical amplitudes and phases have enabled *ab initio* analysis of EXAFS data,[30] although some limitations in derived coordination numbers and distances have been found.[31]

Some of us have developed a new integrated approach to the analysis of EXAFS data based on full curved-wave, multiple-scattering theoretical analysis. The GNXAS approach[32] provides for direct fitting of theoretical signals (calculated by utilizing Hedin–Lundqvist complex exchange and correlation potentials[33])-to the experimental data. It incorporates single- and multiple-scattering signals with proper treatment of correlated distances and Debye–Waller (DW) factors. GNXAS has now been evaluated on several simpler systems (including SiX_4 (X = F, Cl,

(16) Burgess, B. K. *Chem. Rev.* **1990**, *90*, 1377.
(17) Snyder, B. S.; Holm, R. H. *Inorg. Chem.* **1988**, *27*, 2339.
(18) Reynolds, M. S.; Holm, R. H. *Inorg. Chem.* **1988**, *27*, 4494.
(19) Noda, I.; Snyder, B. S.; Holm, R. H. *Inorg. Chem.* **1986**, *25*, 3851.
(20) (a) Kim, J.; Rees, D. C. *Science* **1992**, *257*, 1677; *Nature* **1992**, *360*, 553. See also: (b) Chan, M. K.; Kim, J.; Rees, D. C. *Science* **1993**, *260*, 792.
(21) Mo K-edge XAS: (a) Eidsness, M. K.; Flank, A.-M.; Smith, B. E.; Flood, A. C.; Garner, C. D.; Cramer, S. P. *J. Am. Chem. Soc.* **1986**, *108*, 2746. (b) Flank, A.-M.; Weininger, M.; Mortenson, L. E.; Cramer, S. P. *J. Am. Chem. Soc.* **1986**, *108*, 1049. (c) McLean, P. A.; True, A. E.; Nelson, M. J.; Chapman, S.; Godfrey, M. R.; Teo, B.-K.; Orme-Johnson, W. H.; Hoffman, B. M. *J. Am. Chem. Soc.* **1987**, *109*, 943.
(22) S K-edge and Mo L-edge studies: Hedman, B.; Frank, P.; Gheller, S. F.; Roe, A. L.; Newton, W. E.; Hodgson, K. O. *J. Am. Chem. Soc.* **1988**, *110*, 3798.
(23) Fe K-edge EXAFS: (a) Antonio, M. R.; Teo, B.-K.; Orme-Johnson, W. H.; Nelson, M. J.; Groh, S. E.; Lindahl, P. A.; Kauzlarich, S. M.; Averill, B. A. *J. Am. Chem. Soc.* **1982**, *104*, 4703. (b) Arber, J. M.; Flood, A. C.; Garner, C. D.; Gormal, C. A.; Hasnain, S. S.; Smith, B. E. *Biochem. J.* **1988**, *252*, 421.
(24) (a) Cramer, S. P.; Hodgson, K. O.; Stiefel, E. I.; Newton, W. E. *J. Am. Chem. Soc.* **1978**, *100*, 2748. (b) Cramer, S. P.; Hodgson, K. O. *Prog. Inorg. Chem.* **1979**, *25*, 1. (c) Scott, R. A. *Meth. Enzymol.* **1985**, *117*, 414.
(25) It has long been recognized that MS effects can contribute significantly to EXAFS, including those of inorganic molecules. The effects are particularly evident for 3-body signals when the intervening atom nears a linear relationship with the absorber and a distant scatterer, as occurs, for example, in Fe–oxo dimers[26] and metal carbonyls.[27] Effects can also be quite prominent for certain rigid ligands such as imidazoles and porphyrins.[28] MS effects can be of such magnitude that they contribute significantly to the total EXAFS signal at higher frequencies and in some instances can dominate over single-scattering (χ_2) signals. Such an effect is seen, for example, in $Fe(acac)_3$, where the multiple-scattering contributions of Fe–O–C are comparable in magnitude to those of the direct χ_2 Fe–C contributions, thereby making extraction of reliable empirical Fe–C second-shell parameters impossible.[29] Improvements in codes for theoretical calculations now enable these effects to be explicitly included[30] and thus evaluated as to their relative importance in heterometal cluster EXAFS, as is done in this work.
(26) Co, M. S.; Hendrickson, W. A.; Hodgson, K. O.; Doniach, S. *J. Am. Chem. Soc.* **1983**, *105*, 1144.
(27) Filipponi, A.; Di Cicco, A.; Zanoni, R.; Bellatreccia, M.; Sessa, V.; Dossi, C.; Psaro, R. *Chem. Phys. Lett.* **1991**, *184*, 485.
(28) (a) Co, M. S.; Scott, R. A.; Hodgson, K. O. *J. Am. Chem. Soc.* **1981**, *103*, 986. (b) Hasnain, S. S.; Strange, R. W. In *Synchrotron Radiation and Biophysics*; Hasnain, S. S., Ed.; Ellis Horwood: Chichester, U.K., 1990; Chapter 4 and references therein.
(29) Westre, T. E.; Di Cicco, A.; Filipponi, A.; Natoli, C. R.; Solomon, E. I.; Hedman, B.; Hodgson, K. O. To be submitted to *J. Am. Chem. Soc.*
(30) (a) Tyson, T. A.; Hodgson, K. O.; Natoli, C. R.; Benfatto, M. *Phys. Rev. B* **1992**, *46*, 5997. (b) Mustre de Leon, J.; Rehr, J. J.; Zabinsky, S. I.; Albers, R. C. *Phys. Rev. B* **1991**, *44*, 4146. (c) Rehr, J. J.; Albers, R. C. *Phys. Rev. B* **1990**, *41*, 8139. (d) Brouder, C.; Ruiz-Lopez, M. F.; Pettifer, R. F.; Benfatto, M.; Natoli, C. R. *Phys. Rev. B* **1989**, *39*, 1488. (e) Binsted, N.; Cook, S. L.; Evans, J.; Greaves, G. N.; Price, R. J. *J. Am. Chem. Soc.* **1987**, *109*, 3669. (f) Natoli, C. R.; Benfatto, M. *J. Phys. (Paris) Colloq.* **1986**, *47*, C8–11. (g) Gurman, S. J.; Binsted, N.; Ross, I. J. *J. Phys.* **1986**, *C19*, 1845.
(31) Vaarkamp, M.; Dring, I.; Oldman, R. J.; Stern, E. A.; Koningsberger, D. C. *Phys. Rev. B*, submitted for publication and presented at XAFS VII.
(32) (a) Filipponi, A.; Di Cicco, A.; Tyson, T. A.; Natoli, C. R. *Solid State Commun.* **1991**, *78*, 265. (b) Filipponi, A.; Di Cicco, A. *Synch. Rad. News* **1993**, *6*, 13.
(33) Hedin, L.; Lundqvist, S. *Solid State Phys.* **1969**, *23*, 1.

CH_3),[34] $Os_3(CO)_{12}$,[27] Br_2 and HBr,[35] and brominated hydrocarbons[36]); the approach should offer several distinct advantages for EXAFS analysis of heterometal clusters and other inorganic complexes.

We report here further investigations of cluster assembly reactions in THF solution and structural characterizations of cluster products $MFe_4S_6(PEt_3)_4Cl$ (M = Mo, V). Further, we describe the first application of GNXAS to a relatively complicated inorganic cluster, $MoFe_4S_6(PEt_3)_4Cl$, analyzing EXAFS data at both the Mo K and Fe K edges. The metrical details so obtained are compared with the crystallographic values, and the advantages and limitations of this new approach for EXAFS data analysis of heterometal cubane-type clusters are discussed. As will be seen, clusters prepared in this work contain a substantial portion of the KR cofactor model.

Experimental Section

Preparation of Compounds. All operations were performed under a pure dinitrogen atmosphere. Solvents were freshly distilled from appropriate drying agents and were degassed prior to use. $MoCl_3(THF)_3$,[37] $VCl_3(THF)_3$,[38] and $FeCl_2(PEt_3)_2$[17] were prepared as described except that Et_2O was used as the solvent in the preparation of the last compound. All solvent removal steps were performed in vacuo.

$MoFe_4S_6(PEt_3)_4Cl$ (7). $MoCl_3(THF)_3$ (2.8 g, 6.68 mmol) was dissolved in 150 mL of THF, and the solution was heated to 50 °C. Addition of 6.0 mL (29 mmol) of $(Me_3Si)_2S$ to the stirred solution caused a color change from orange to dark purple over 10 min. A solution of 1.70 g (13.4 mmol) of $FeCl_2(PEt_3)_2$ in 50 mL of THF was added dropwise, resulting in a rapid color change to black. At this point, a small aliquot was withdrawn and evaporated to dryness. The ^1H NMR spectrum of the residue dissolved in $CDCl_3$ revealed two major products, the product cluster and $Fe_6S_6(PEt_3)_4Cl_2$[17] in a 7:1 mol ratio, as well as several minor products. The reaction mixture was taken to dryness, and the residue was dissolved in a minimal volume (*ca.* 40 mL) of THF/acetonitrile (3:1 v/v). This solution was loaded on a column (4 × 18 cm) of SX-8 Bio-Beads (Bio-Rad) which had been pretreated by immersion in THF overnight. The column was eluted with THF. The first band (brown) was discarded. The second band (green-brown) was collected and evaporated to give a black powder, which was dissolved in 150 mL of ether/acetonitrile (5:1 v/v). Slow solvent reduction followed by cooling at −20 °C overnight resulted in the separation of 1.42 g (42%) of pure product as black crystals. ^1H NMR ($CDCl_3$): δ 1.55 ($MoPCH_2CH_3$), 0.91 ($FePCH_2CH_3$), 0.52 ($MoPCH_2$), −2.15 ($FePCH_2$). FAB-MS (3-nitrobenzyl alcohol): M^+ calcd *m/e* 1020.811, found *m/e* 1020.809.

$VFe_4S_6(PEt_3)_4Cl$ (8). $VCl_3(THF)_3$ (1.1 g, 2.9 mmol) was dissolved in 50 mL of THF. Addition of 1.4 mL (6.7 mmol) of $(Me_3Si)_2S$ to the stirred solution caused a color change from orange to dark purple over 10 min. A solution of 2.2 g (6.0 mmol) of $FeCl_2(PEt_3)_2$ in 20 mL of THF was added dropwise, causing a rapid color change to black. A ^1H NMR analysis as above showed the product clusters and $Fe_6S_6(PEt_3)_4Cl_2$ present in a 3:1 mol ratio, together with minor impurities. The reaction mixture was stirred overnight and filtered. The filtrate was taken to dryness, and the residue was dissolved in the minimum volume (*ca.* 40 mL) of THF/acetonitrile (3:1 v/v). The solution was chromatographed as in the preceding preparation. The first band (brown) was discarded. The second band (brown) was collected and the solvent removed to give a black powder, which was dissolved in 30 mL of THF/Me_2SO (3:1 v/v). Slow solvent removal overnight resulted in separation from the solution of 0.20 g (14%) of pure product as black crystals. ^1H NMR ($CDCl_3$): δ 2.50 ($VPCH_2$), 1.40 ($VPCH_2CH_3$), 0.98 ($FePCH_2CH_3$), −1.74 ($FePCH_2CH_3$). FAB MS (3-nitrobenzyl alcohol): M^+ calcd *m/e* 973.850, found *m/e* 973.850.

Collection and Reduction of X-ray Data. Black parallelpiped crystals of **7** and **8** were obtained from hexane/THF solutions (3:1 v/v) maintained at −4 °C. Crystals were transferred under a dinitrogen atmosphere into a layer of Paratone-N oil and mounted as described previously.[39,40] Data were collected using graphite-monochromatized Mo Kα radiation on a Siemens R3m/v (**8**) or a Nicolet P3F (**7**) four-circle automated diffractometer equipped with a cryostat operating at 173 K. Following preliminary indexing, refined unit cell parameters were obtained by least-squares fits of 34 (**7**) or 33 (**8**) machine-centered reflections with $5° \le 2\theta \le 30°$; the rhombohedral cell was transformed to the hexagonal setting for data collection. Data sets were processed and corrected for Lorentz and polarization effects with a locally-modified version of XDISK (SHELXTL program suite, Siemens XRD Corp., Madison, WI); empirical absorption corrections (XEMP) were applied, using azimuthal ψ-scan data for **8**. Three check reflections monitored every 97 reflections showed no significant decay over the course of data collection. Crystallographic data are summarized in Table I.

Table I. Crystallographic Data[a] for $MoFe_4S_6(PEt_3)_4Cl$ (**7**) and $VFe_4S_6(PEt_3)_4Cl$ (**8**)

	7	**8**
formula	$C_{24}H_{60}ClFe_4MoP_4S_6$	$C_{24}H_{60}ClFe_4P_4S_6V$
fw	1019.87	974.75
cryst system	trigonal	trigonal
space group	$R\bar{3}c$	$R\bar{3}c$
Z	12	12
a, Å	13.017(3)	12.994(2)
c, Å	92.98(3)	92.58(1)
V, Å^3	13644(7)	13434(4)
ρ_{calc}, g/cm^3	1.49	1.45
T, K	173	173
μ, mm^{-1}	2.00	1.96
R^b (R_w^c), %	4.64 (4.79)	6.84 (5.05)

[a] All data collected with graphite–monochromatized Mo Kα radiation (λ = 0.710 69 Å) using ω-scans. [b] $R = \sum||F_o|-|F_c||/\sum|F_o|$. [c] $R_w = \{\sum[w(|F_o| - |F_c|)^2]/\sum(w|F_o|^2)\}^{1/2}$, with the weighting scheme provided by a 3-term Chebyshev polynomial: Carruthers, J. R.; Watkin, D. J. *Acta Crystallogr.* **1979**, *A35*, 698.

Structure Solutions and Refinements. The initial structure of compound **7** was obtained by direct methods (XS from the SHELXTL package). Axial photographs and intensities of symmetry-equivalent reflections indicated $3m$ Laue symmetry for **7**. Systematic absences further narrowed the choice of space group to $R3c$ (No. 161) or $R\bar{3}c$ (No. 167), with simple E statistics suggesting a centrosymmetric cell. The positions of Mo, Fe, S, and P atoms were furnished by direct methods in $R\bar{3}c$; the choice of the proper space group was confirmed by successful refinement to convergence. Intensity data for compound **8** implied a structure isomorphous with that of **7**, a matter corroborated by successful refinement using the atom coordinates of **7** as a trial structure. Atoms not initially located by direct methods were found by successive Fourier or difference Fourier maps with intervening cycles of full-matrix least-squares refinements (CRYSTALS, with graphical interface provided by XP from SHELXTL). All non-hydrogen atoms were treated anisotropically; in the final stages of the refinements, hydrogen atoms were placed at calculated positions 0.96 Å from, and with isotropic thermal parameters 1.2× those of, the bonded carbon atoms. For both structures, the ethyl group of the Et_3P ligand on the C_3 axis shows excessive thermal motion, probably due to disorder resulting from the symmetry constraints imposed by the special position. No satisfactory model for the disorder was found; consequently, bond distances of the disordered group are anomalous. Final difference Fourier maps revealed peaks of *ca.* 1–2 e/Å^3 intensity close to the 32 (D_3) position. Because of uncertainties concerning the presence of solvent in the lattice, no attempt was made to model this feature. Final R-values are given in Table I.[41]

Collection and Reduction of X-ray Absorption Spectroscopy Data. Solid samples of **7** were ground to a fine powder and diluted with BN, pressed into a fine pellet, and sealed between Mylar (Mo K-edge) or Kapton (Fe K-edge) tape, in an aluminum spacer. Samples were prepared in an inert (N_2) box. The samples were frozen in liquid nitrogen upon removal from the box, and the measurements were performed at 10 K using an Oxford Instruments CF1208 continuous-flow liquid-helium cryostat. Transmission X-ray absorption spectroscopic data were collected at the Stanford

(34) Di Cicco, A.; Stizza, S.; Filipponi, A.; Boscherini, F.; Mobilio, S. *J. Phys. B* **1992**, *25*, 2309.
(35) D'Angelo, P.; Di Cicco, A.; Filipponi, A.; Pavel, N. V. *Phys. Rev. A* **1993**, *47*, 2055.
(36) Burattini, E.; D'Angelo, P.; Di Cicco, A.; Filipponi, A.; Pavel, N. V. *J. Phys. Chem.*, in press.
(37) (a) Dilworth, J. R.; Richards, R. L. *Inorg. Synth.* **1980**, *20*, 119. (b) Dilworth, J. R.; Zubieta, J. *Inorg. Synth.* **1986**, *24*, 193.
(38) Manzer, L. E. *Inorg. Synth.* **1982**, *21*, 138.
(39) Hope, H. In *Experimental Organometallic Chemistry*; ACS Symposium Series 357; American Chemical Society: Washington, DC, 1987; Chapter 10.
(40) Lee, S. C.; Li, J.; Mitchell, J. C.; Holm, R. H. *Inorg. Chem.* **1992**, *31*, 4333.
(41) See paragraph at the end of this article concerning supplementary material.

Synchrotron Radiation Laboratory (SSRL) unfocused beam line 7-3, under 3 GeV and 40–80 mA conditions. Measurements at the Mo K and Fe K absorption edges were performed using a Si(220) double-crystal monochromator, with Ar and N_2 ionization chamber gases, respectively. Internal energy calibration[42] was used by insertion of a foil (Mo or Fe) between the second and third ionization chambers. The data represent the average of 8 (Mo) and 4 (Fe) individual scans. The effects of a quartet from a monochromator glitch were removed in the Fe K-edge data (at around k = 11.8, 12.1, 12.3, and 12.6 Å^{-1}). Careful inspection of individual and averaged I_0 signals for the Mo K-edge data revealed a very small but consistent dip and step at about k = 14 Å^{-1} (see text for further comments).

Analysis of X-ray Absorption Spectroscopy Data. EXAFS data were analyzed using the program package GNXAS. The theoretical basis for this approach has been described elsewhere,[32] and several applications to simple molecular systems have been published.[27,34-36] A detailed description of fitting methodologies and strategies, in particular involving three-body MS signals and the effects of multiple excitations (not found to be as important in the cases treated here), will be published for Fe(acac)$_3$ and K_3[Fe(CN)$_6$].[29] Parameters relevant to the specific calculations are given below.

Phase shifts were calculated within the standard muffin-tin approximation using the entire cluster 7 (including C atoms) and up to an energy limit of 100 Ry (1360 eV) above the Mo K/Fe K edges. The Mattheiss prescription[43] of overlapping, self-consistent atomic charge densities of the atoms of the cluster was used to construct the Coulomb part of the effective one-electron potential, whereas the Hedin–Lundqvist plasmon-pole approximation was used to model its exchange and correlation parts. The imaginary part of the latter takes into account extrinsic inelastic processes of the photoelectron on its way out of the system and models *a priori* its mean-free path. The muffin-tin radii were chosen by scaling Norman radii[44] of the cluster atoms by a factor of about 0.8 in such a way as to match the nearest neighbor distance. Angular momentum values up to l = 22 were used for the Mo atom, and smaller limits were sufficient for the lighter atoms. EXAFS signals corresponding to the various coordination shells were calculated out to a 5-Å cutoff around the absorbing atom(s). In the cluster there are two types of Fe absorbers (with somewhat different geometric environments); thus, at the Fe K-edge the total EXAFS signal was calculated in two parts and weighted together using the proper ratios. The EXAFS signals included contributions from 2-body and 3-body configurations. Within each n-body configuration (n = 2, 3), all MS contributions were taken into account. Possible 3-body MS signals were calculated theoretically and fits were performed, but their contributions were found not to be significant for either the Mo-K or Fe-K EXAFS data. The criteria used are discussed elsewhere in more detail (see text).

The least-squares fits were performed on the averaged energy-calibrated, raw absorption data without prior background subtraction or Fourier filtering. The total model signal $\alpha(k)$ was calculated from the indicated relationship

$$\alpha(k) = J\sigma_0(k)(1 + \chi(k)) + \beta(k)$$

where J is the edge jump, $\sigma_0(k)$ is the theoretical atomic-like background (containing no EXAFS contribution) modeled within the hydrogenic approximation, $\chi(k)$ is the total EXAFS signal, and $\beta(k)$ contains the remaining background effects (experimental—modeled as a polynomial spline—and multiple excitations). The latter is refined during the fitting procedure to minimize the difference between the theoretical and experimental signals. The final splines (a component of $\beta(k)$) used were in three segments of order 4,5,4 (Mo) and 4,4,4 (Fe). The defining energy points were 20 060, 20 230, 20 460, 20 755 eV (Mo) and 7150, 7280, 7530, 7870 eV (Fe).

The structural parameters varied in the refinements were the distance and DW factors for each wave (coordination numbers fixed). Nonstructural parameters included E_0 (which aligns the experimental energy scale to the theoretical one), S_0^2 (a many-body amplitude reduction factor), Γ_c (core-hole lifetime), and E_r (experimental monochromator energy resolution). There are theoretical considerations that can be and have been used to limit the range of variation of these parameters.[30a] In practice, E_0 turns out to be a core ionization threshold (vacuum level) that can be estimated from a non-self-consistent calculation of the potential within an uncertainty of 2–3 eV. There are also good reasons to believe that the variation of S_0^2 is between 0.9 and 1.0, the range in which this parameter was found to vary in all applications thus far. The value of Γ_c was kept fixed to experimentally measured values.[45] Finally, the experimental resolution was allowed to vary by ±(1–2) eV around the expected value.[46] The least-squares fits were done with k^3 weighting. The function minimized was $R = [\sum_i(\alpha_i^{exp}(k_i) - \alpha_i^{theor}(k_i))^2 k_i^n] / [\sum_i(\alpha_i^{exp}(k_i))^2 k_i^n]$, with n = 3, which gives the least-squares residual R. Its expected value for n = 0 is the variance of the experimental data (statistical noise) whose typical values are in the range 10^{-6}–10^{-8}. The final, reported fits were done over the k-range of 3.7–14.0 Å^{-1} (Mo) and 2.9–14.0 Å^{-1} (Fe).

Scheme I. Assembly of Pentanuclear V/Mo–Fe–S Clusters

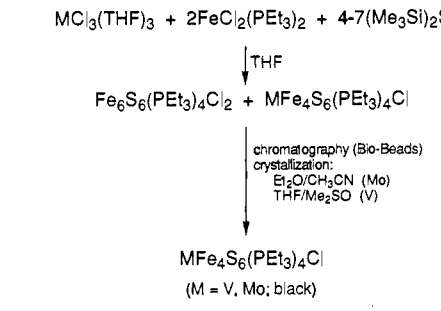

Results and Discussion

Preparation of Compounds. The clusters $MoFe_4S_6(PEt_3)_4Cl$ and $VFe_4S_6(PEt_3)_4Cl$ were prepared by the self-assembly system in Scheme I. These products are always accompanied by the basket cluster $Fe_6S_6(PEt_3)_4Cl_2$, which is easily recognized by its characteristic isotropically shifted ^{1}H NMR spectrum.[17] In typical preparations, the mole ratio $MFe_4S_6(PEt_3)_4Cl$:$Fe_6S_6(PEt_3)_4Cl_2$ is *ca.* 7:1 for M = Mo and 3:1 for M = V, prior to chromatography of the reaction mixture. The latter step was intended to separate components with molecular weights above and below *ca.* 1000 and also provides a partial separation of the two main products. Advantage was taken of the instability of $Fe_6S_6(PEt_3)_4Cl_2$ in Me_2SO, where it is immediately decomposed, and in acetonitrile, where it is completely degraded over several days. Consequently, it was found possible to crystallize pure $MoFe_4S_6(PEt_3)_4Cl$ from ether/acetonitrile and pure $VFe_4S_6(PEt_3)_4Cl$ from THF/Me_2SO. Yields are modest, but the preparations can be executed in a short time (1–2 d). Alternatively, the crude products before chromatography can be purified by fractional crystallization from THF/hexane, but the process is slower and the yields are lower. The clusters were obtained as air-sensitive, highly crystalline black solids soluble in weakly polar organic solvents.

The clusters were identified by a combination of spectroscopic methods and X-ray structural analysis. Comparisons of calculated and observed high-resolution FAB mass spectra in the M^+ parent ion region are presented in Figure 2. The agreement for both compounds across the entire isotope distribution pattern is excellent and unambiguously establishes the stoichiometries. Further, for both, relatively intense peaks were observed in low-resolution spectra at the masses $M^+ - 118n$, corresponding to ions that have successively lost n = 1, 2, and 3 Et_3P ligands. The isotropically shifted ^{1}H NMR spectra of both compounds, set out in Figure 3, reveal two types of phosphine ligands in a 3:1 ratio. These spectra were always observed in products of different preparations and in different samples of the same product. As will be seen, they are consistent with the structures of the clusters in the solid state.

(42) Scott, R. A.; Hahn, J. E.; Doniach, S.; Freeman, H. C.; Hodgson, K. O. *J. Am. Chem. Soc.* **1982**, *104*, 5364.
(43) Mattheiss, L. F. *Phys. Rev.* **1969**, *181*, 987.
(44) Norman, J. G. *Mol. Phys.* **1976**, *81*, 1191.
(45) Krause, M. O.; Oliver, J. H. *J. Phys. Chem. Ref. Data* **1979**, *8*, 329.
(46) The experimental energy resolution is determined by the specific optics of the beam line. The principal determining factor is the monochromator, with the resolution determined by the relationship $\Delta E/E = \cot(\theta)\cdot\Delta\theta$, where θ is the setting angle of the monochromator at the particular edge and $\Delta\theta$ is a function of the Darwin width and the vertical angular acceptance of the monochromator. The values at the Mo K and Fe K edges for the experimental conditions used for these measurements were 5.5 (Mo) and 1.0 (Fe) eV.

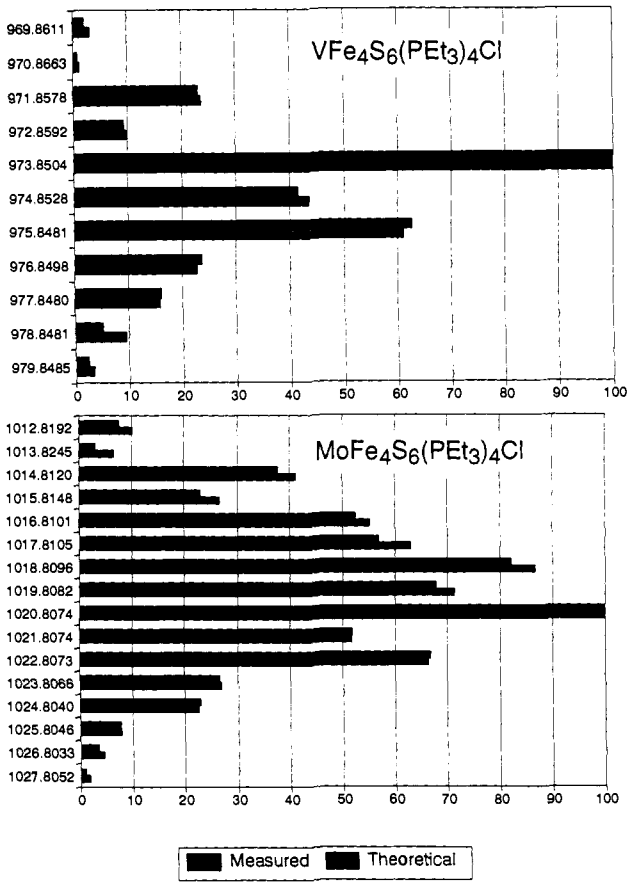

Figure 2. Comparison of measured (lower) and theoretical (upper) FAB-mass spectra in the parent ion (M^+) regions of $VFe_4S_6(PEt_3)_4Cl$ and $MoFe_4S_6(PEt_3)_4Cl$ in 3-nitrobenzyl alcohol. Masses are experimental values; the most intense peak in each spectrum has been scaled to 100.

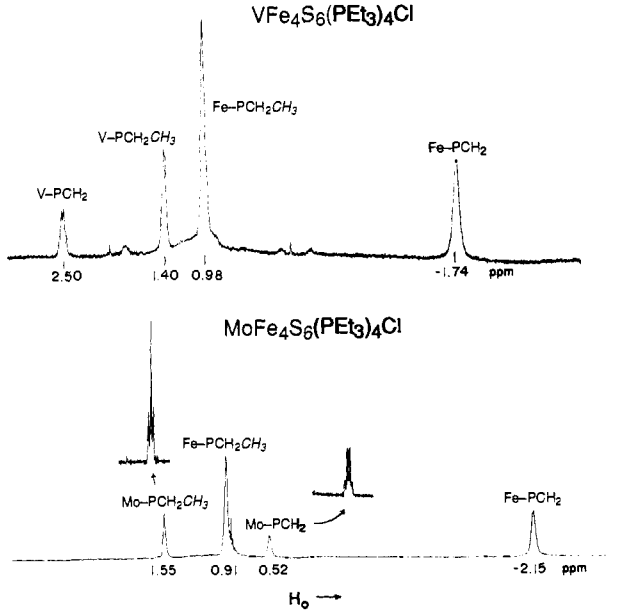

Figure 3. ^1H NMR spectra of $VFe_4S_6(PEt_3)_4Cl$ (300 MHz) and $MoFe_4S_6(PEt_3)_4Cl$ (500 MHz) in $CDCl_3$ solutions at 295 K. Signal assignments are indicated.

Cluster Structures. The structures of $MoFe_4S_6(PEt_3)_4Cl$ and $VFe_4S_6(PEt_3)_4Cl$ determined by X-ray diffraction are introduced in Figure 4. The two clusters are isostructural and nearly isometric and present a new type of cluster topology but, as will be seen, one that is related to previously observed core structures. For this reason, a stereoview is provided in Figure 5. The structures

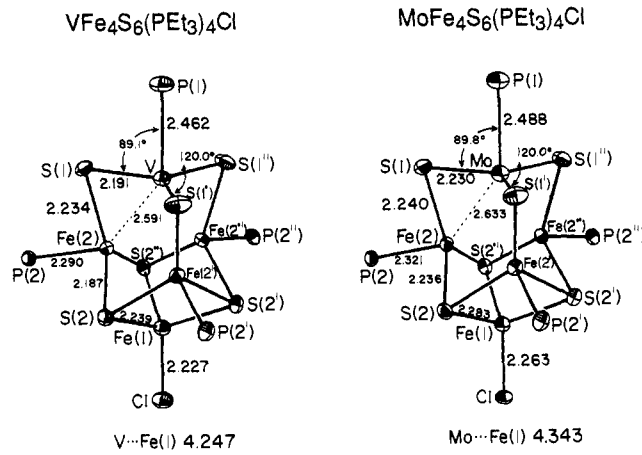

Figure 4. Structures of $MFe_4S_6(PEt_3)_4Cl$ (M = V, Mo) showing the atom-labeling scheme, 50% probability ellipsoids, and selected interatomic distances and bond angles. Primed and unprimed atoms are related by a C_3 axis containing atoms M and Fe(1); ethyl groups are omitted.

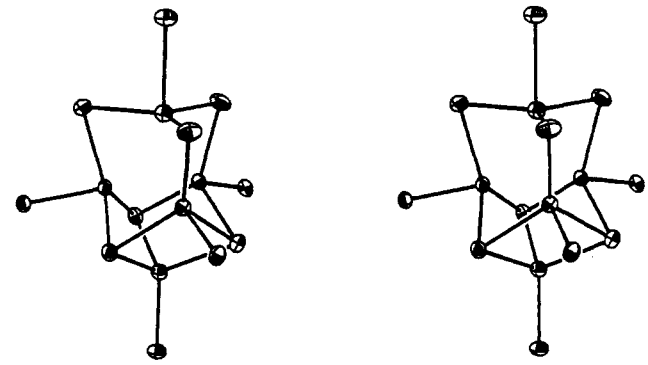

Figure 5. Stereoview of the structure of $MFe_4S_6(PEt_3)_4Cl$ (M = V, Mo).

have crystallographically imposed C_3 symmetry. Among independent metric features, there are 11 bonded distances and 16 bonded angles of interest; these are collected in Table II.

The two molecules contain essentially congruent Fe_4S_3 cuboidal fragments in which Fe(1) carries a terminal chloride ligand and is located in a distorted tetrahedral site with Cl–Fe(1)–S = 115° and S–Fe(1)–S = 103°. Each of the remaining atoms Fe(2,2′,2″) has a terminal Et_3P ligand and exhibits unusual distorted trigonal pyramidal coordination with a phosphorus atom at the apex and three sulfur atoms forming the base. The "perpendicular" angles P(2)–Fe(2)–S(1) = 86–88° and P(2)–Fe(2)–S(2,2″) = 93–98°. The Fe(2) atom is displaced 0.08 Å from the S(1,2,2″) plane in the direction of P(2). Angles in the Fe(2)S(1,2,2″) near-planar units, depicted as **9** (M = V) and **10** (M = Mo), divide into

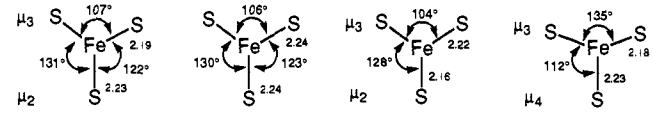

9 **10** **11** **12**

S(1)–Fe(2)–S(2,2″) = 122–131° and S(2)–Fe(2)–S(2′) = 106–107°. The latter angle is within a Fe_2S_2 rhomb of the Fe_4S_3 fragment and compares with S–Fe(1)–S = 103° at the base of fragment. These values conform to the usual range of 103–107° for S–Fe–S angles of Fe_4S_4 cubane-type clusters and emphasize the cuboidal nature of the fragment, whose dimensions are unexceptional.

The remaining coordination position of atoms Fe(2,2′,2″) is occupied by a μ_2-S atom (S(1,1′,1″)), which in turn coordinates the heterometal atom, whose remaining binding site is occupied by the P(1) phosphine ligand. These MS_3P units form trigonal

Table II. Selected Interatomic Distances (Å) and Angles (deg) for $MFe_4S_6(PEt_3)_4Cl$ (M = V, Mo)

dist/angle	M = V	M = Mo
M–P(1)	2.462(3)	2.488(4)
M–S(1)	2.191(1)	2.230(2)
M–Fe(2)	2.591(1)	2.633(2)
M–Fe(1)	4.247(2)	4.343(2)
Fe(1)–Cl	2.227(2)	2.263(4)
Fe(1)–S(2)	2.239(1)	2.283(2)
Fe(1)–Fe(2)	2.638(1)	2.709(2)
Fe(2)–P(2)	2.290(2)	2.321(2)
Fe(2)–S(1)	2.234(1)	2.240(2)
Fe(2)–S(2)	2.187(1)	2.231(2)
Fe(2)–S(2″)	2.190(1)	2.236(2)
Fe(2)–Fe(2′)	2.643(1)	2.694(2)
P(1)–M–S(1)	89.14(5)	89.79(7)
S(1)–M–S(1′)	119.98(1)	120.00(1)
Fe(2)–M–Fe(2′)	61.32(4)	61.54(5)
Cl–Fe(1)–S(2)	115.11(4)	115.50(7)
S(2)–Fe(1)–S(2′)	103.29(5)	102.83(8)
Fe(2)–Fe(1)–Fe(2′)	60.12(3)	59.62(6)
P(2)–Fe(2)–S(1)	86.08(6)	87.69(9)
P(2)–Fe(2)–S(2)	97.63(6)	96.1(1)
P(2)–Fe(2)–S(2″)	94.30(5)	93.53(9)
S(1)–Fe(2)–S(2)	121.83(6)	123.0(1)
S(1)–Fe(2)–S(2″)	131.03(6)	130.4(1)
S(2)–Fe(2)–S(2″)	106.68(7)	106.1(1)
M–S(1)–Fe(2)	71.69(6)	72.17(8)
Fe(1)–S(2)–Fe(2)	73.18(5)	73.76(8)
Fe(1)–S(2)–Fe(2′)	73.11(5)	73.67(8)
Fe(2)–S(2)–Fe(2′)	74.30(5)	74.19(9)

planar fragments that much more closely approach local C_{3v} symmetry than do FeS_3P fragments. Here we find P(1)–M–S(1) = 89–90° and S(1)–M–S(1′) = 120°; deviations from the S(1,1′,1″) planes are 0.033 Å (V) and 0.007 Å (Mo), both away from P(1). The M–Fe(2) separations of 2.591(1) Å (V) and 2.633(2) Å (Mo) indicate the likelihood of direct metal–metal interactions. The ratios of long and short M–Fe interactions (Figure 4) are 1.61 (V) and 1.60 (Mo), emphasizing the elongated nature of the nearly identical core structures. Trigonal pyramidal coordination is unprecedented for vanadium and molybdenum in any oxidation state. Because of this, we do not attempt to infer oxidation state from bond distances.

Cluster Topologies. In our topological method for clusters containing four-coordinate M sites,[47] $MFe_4S_6(PEt_3)_4Cl = M_5Q_6L_5$ and has the bridging modality $[n_2n_3n_4]$ = [330], in which the numbers of doubly, triply, and quadruply bridging Q atoms are specified. Under the condition of uniterminal ligation,[47] there is only one other possible bridging modality, [411], but to our knowledge no such structure has been found experimentally. Indeed, pentanuclear metal–chalcogenide clusters are extremely rare. The present clusters can be understood as one member of a topological set of five clusters that are related by the formal process of metal-capping of a trigonal S_3 face. The concept is presented in Figure 6 in terms of core structures that are oriented so as to bring all into a common perspective. Capping of the unknown but seemingly viable tetrahedral core [600]-M_4S_6 on the S(456) face with atom M(5) affords the present clusters [330]-$M_5Q_6L_5$. Repetition of process affords [141]-M_6S_6 (basket cluster), then [033]-M_7S_6, and finally [006]-M_8S_6, the only possible topology for this formula. The last two structures may also be visualized as mono- and bicapped prismanes derived from [060]-M_6S_6.

As shown in Table III, there are realized examples of M_5 through M_8 clusters with these topologies.[17-19,48-54] All known examples of [330]-M_5S_6, [141]-M_6S_6, and [033]-M_7S_6 contain

GENERATION OF HIGHER-NUCLEARITY STRUCTURES BY FACE-CAPPING OF TETRAHEDRAL M_4S_6

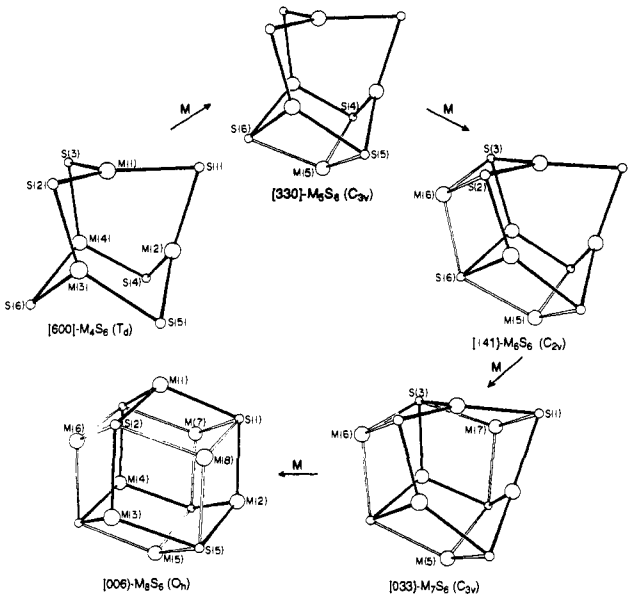

Figure 6. Schematic depiction of the core conversion sequence $M_4S_6 \rightarrow M_5S_6 \rightarrow M_6S_6 \rightarrow M_7S_6 \rightarrow M_8S_6$ effected by capping of S_3 faces by M atoms. Bridging modalities $[n_2n_3n_4]$ and idealized symmetries are indicated. The structures of M_6S_6,[17] M_7S_6,[19] and M_8S_6[51] were drawn using atomic coordinates of clusters with M = Fe. Coordinates for M_5S_6 were taken from this work; M_4S_6 is an unknown species.

Table III. Clusters with Cores Conceptually Interrelated by Face-Capping Reactions Based on [600]-M_4S_6

core	clusters	ref
[600]-M_4S_6	unknown	
[330]-M_5S_6	$MFe_4S_6(PEt_3)_4Cl$ (M = V, Mo)	this work
↓		
[141]-M_6S_6	$Fe_6S_6(PR_3)_4X_2$ (X = halide, RS^-), $[Fe_6S_6(PEt_3)_6]^+$	17, 18, 48
↓		
[033]-M_7S_6	$Fe_7S_6(PEt_3)_4Cl_3$, $Co_7S_6(PPh_3)_4X_3$, $Co_7S_6(PPh_3)_5Cl_2$	19, 49, 50
↓		
[006]-M_8S_6	$[Fe_8S_6I_8]^{3-}$, $[Co_8S_6(SPh)_8]^{4-,5-}$, $Ni_8S_6(PPh_3)_6Cl_2$, $Ni_8S_6(PPh_3)_8$	51, 52, 53, 54

iron sites with terminal phosphine ligands, some or all of which exhibit trigonal pyramidal coordination. All such sites in $MFe_4S_6(PEt_3)_4Cl$ (**9**, **10**), the four sites in $Fe_6S_6(PR_3)_4X_2$,[17,18] four of the six sites in $[Fe_6S_6(PEt_3)_6]^+$,[48] and three of the four sites in $Fe_7S_6(PEt_3)_4Cl_3$[19] have this stereochemistry. Average dimensions for basket clusters and the heptanuclear species are shown in **11** and **12**, respectively. The latter differs from **9–11** in that all sulfur atoms are integrated into Fe_2S_2 rhombs whereas in the other units the μ_2-S atoms are not in rhombs. The close structural correspondence between **11** and **9**/**10** in the present clusters is quite apparent. All sites with chloride terminal ligands in any iron–sulfur cluster are tetrahedral. Consequently, it is probable that the geometries of the $M_{5-7}S_6$ members of the set in Figure 6 owe their existence to phosphine ligation. The structures of $MFe_4S_6(PEt_3)_4Cl$ and the KR cofactor model **6** are compared in a subsequent section.

(47) You, J.-F.; Holm, R. H. *Inorg. Chem.* **1992**, *31*, 2166. Each bridging modality is degenerate in that it corresponds to more than one atom connectivity pattern. Uniterminal ligation requires that each M atom has only one terminal ligand.

(48) Snyder, B. S.; Holm, R. H. *Inorg. Chem.* **1990**, *29*, 274.

(49) Jiang, F.; Huang, L.; Lei, X.; Liu, H.; Kang, B.; Huang, Z.; Hong, M. *Polyhedron* **1992**, *11*, 361.

(50) Fenske, D.; Hachgenei, J.; Ohmer, J. *Angew. Chem., Int. Ed. Engl.* **1985**, *24*, 706.

(51) Pohl, S.; Saak, W. *Angew. Chem., Int. Ed. Engl.* **1984**, *23*, 907. For a related example, *cf.*: Saak, W.; Pohl, S. *Angew. Chem., Int. Ed. Engl.* **1991**, *30*, 881.

(52) Christou, G.; Hagen, K. S.; Bashkin, J. K.; Holm, R. H. *Inorg. Chem.* **1985**, *24*, 1010.

(53) Fenske, D.; Ohmer, J. *Angew. Chem., Int. Ed. Engl.* **1987**, *26*, 148.

(54) Fenske, D.; Magull, J. *Z. Naturforsch. B* **1990**, *45b*, 121.

Table IV. Results from GNXAS Fits to the Mo K-Edge Data of $MoFe_4S_6(PEt_3)_4Cl$[a]

bond	cryst dist (Å)	R[b] (Å) (DW[c] (Å^2))	R (Å) (DW (Å^2))	R (Å) (DW (Å^2))
Mo–S(1)	2.230	2.243 (0.0041)	2.234 (0.0055)	2.236 (0.0047)
Mo–P(1)	2.488	2.509 (0.0091)	2.489 (0.0100)	2.490 (0.0100)
Mo–Fe(2)	2.633	2.629 (0.0040)	2.630 (0.0067)	2.628 (0.0061)
Mo–C(1)	3.657		3.615 (0.0045)	3.610 (0.0082)
Mo–S(2)	3.942		3.941 (0.0058)	3.925 (0.0044)
Mo–C(2)	4.049		4.070 (0.0049)	4.070 (0.0098)
Mo–Fe(1)	4.343			4.310 (0.0043)
Mo–P(2)	4.675			4.640 (0.0097)
R-value[d]		3.93×10^{-6}	1.80×10^{-6}	1.46×10^{-6}

[a] The three final fits from successive inclusion of outer shell two-body contributions are given. The total number of points in the fitting range k = 3.7–14.0 Å^{-1} was 240. [b] R = interatomic distance. [c] DW = Debye–Waller factor. [d] Least-squares residual: see text.

EXAFS Structural Analysis. The approach in GNXAS calculations is to fit the total experimental, non-Fourier-filtered EXAFS data (without prior background subtraction). The first step in this investigation was to calculate model EXAFS signals for each shell, on the basis of crystallographic distances and reasonable DW factors, for 2-body contributions within a 5-Å cutoff. This enabled a determination as to which waves should be the major contributors to the experimental EXAFS. Initially, those waves that contributed most significantly were included and refined *vs* the experimental data. The significance of incremental inclusions of additional waves was monitored in the quality of fits (R-factors). As a further important indicator, the residuals of the total EXAFS signal and the Fourier transform as well as individual contributions to the EXAFS signal and their Fourier transforms were examined.

The distances and DW factors were allowed to vary within preset ranges, typically ±0.05 Å and ±0.05 Å^2, respectively. The results were carefully monitored to ensure that all parameters refined inside the allowed ranges. The weight in the refinement, k^3 *vs* k^4, was systematically tested, and for both data sets k^3 was found to give the most accurate and consistent results. Spline evaluations using 2, 3, and 4 regions and varying the orders from 2 to 5 were also carried out, with the best results judged from low, smooth residual background as well as the magnitude of low-R Fourier transform components.

It was apparent from the background subtraction/spline fit routine that there was a step in the Mo K-edge data near k = 14 Å^{-1} causing a small but significant abnormality in the amplitude envelope. Inspection of the I_0 signal (average as well as individual scans) revealed a trough followed by a small step at this location in k. Attempts to eliminate this background abnormality by introducing and refining a simulated multiple excitation step at this energy were not successful, and the data were therefore truncated at k = 14 Å^{-1}. Its detection shows, however, the powerful nature and usefulness of the background subtraction routine.

Mo K-Edge Results. (a) First Shell. These results for $MoFe_4S_6(PEt)_4Cl$ are given in Table IV. The EXAFS data and fits, including the residual, are presented in Figure 7, and Fourier transforms, including the transforms of the residuals, are shown in Figure 8. Individual EXAFS are set out in Figure 9, and individual Fourier transform contributions, in Figure 10. The low-R EXAFS is dominated by three waves from strong backscatterers at 2.230 Å (Mo–S), 2.488 Å (Mo–P), and 2.633 Å (Mo–Fe), as seen in Figure 10. The EXAFS distances for these three shells show excellent agreement with the crystallographic values, deviating by <0.01 Å. Over a large number of fits with different k-ranges and background parameters, the Mo–S, Mo–P, and Mo–Fe distances were remarkably constant. The largest variation in any of them from the crystallographic distance is 0.03 Å; this was, however, a case with correlation problems and one where the DW factors were not well-behaved.

(b) Outer Shells. As would be expected, contributions from the further shells were smaller in magnitude and contributed less significantly to the total EXAFS signal. In the 3–4-Å range, there are waves from C(1), S(2), and C(2) at 3.657, 3.942, and 4.049 Å, respectively. Of these, as can be seen in Figure 9, only the signal from S(2) is relatively large, as confirmed by the consistently better determined Mo–S(2) distance. The largest variation seen in this distance was 0.03 Å, whereas that for the two Mo–C distances was 0.05 Å (Table IV). Atoms C(1) and C(2) are those which show disorder in the crystal structure and thus are less well determined. Their DW factors (0.008 and 0.010 Å^2) are almost twice as large as that for S(2).

The next two shells, from Fe(1) (4.343 Å) and P(2) (4.675 Å), both show higher signals than the C shells (Figure 9). The long Mo–Fe(1) distance also shows a somewhat larger error, deviating by as much as 0.04 Å from the crystallographic value. In addition, the P signal shows a relatively large DW factor. The signal from the long Mo–Fe(1) distance refined consistently to a more normal DW factor and when included in the fit gave a small improvement in the residual. Comparison of Figures 8 and 10 reveals that this signal is the main contributor in the region of the Fourier transform at about 3.6–4.0 Å (and is the main contributor to the small peak at 3.9 Å). When the Fe–Mo wave is omitted, this region of the transform is not at all well fit, whereas with it the region is quite well reproduced. Therefore, it is clear that the long Mo–Fe(1) distance does contribute a small but significant amount to the total EXAFS signal. However, we caution that the total signal is dominated by the first three shells and that the inclusion of the additional five outer shells reduces the R-value only from 3.93×10^{-6} to 1.46×10^{-6}.

(c) 3-Body Signals. The presence of these signals was evaluated by calculating their theoretical forms for distances up to 5 Å in $MoFe_4S_6(PEt)_4Cl$. There are 14 unique 3-body pathways, which range in total distance from 3.552 to 4.995 Å. The shortest pathway involves Mo–Fe(2)–S(1) and has an intervening angle of 72°. The largest angle is 140° at 4.815 Å. Comparison of the magnitudes of the 3-body signals with those of the 2-body signals revealed that most of them would not make significant contributions to the total EXAFS signal. However, fits were attempted by adding the five most intense signals (Mo–P(1)–C(1), Mo–S(1)–S(1′), Mo–Fe(2)–S(2), Mo–Fe(2)–Fe(1), Mo–Fe(2)–P(2)) to the eight 2-body pathways. The 3-body pathways were included as the two shortest bonds and their intervening angle; thus, the longest distance was not an independent parameter in the fit. Each triangular path introduced nine variables to be fitted: two distances, one angle, and the six elements of the covariance matrix of the molecular vibrations of the three atoms. Because 3-body pathways include (or are functions of) some of the pathways from the previous 2-body pathway fits, the increase in the number of varied parameters was only from 19 to 43. Only the path Mo–Fe(2)–P(2) was found to have an intensity comparable to the 2-body signals from a distant shell (Mo–S(2), Mo–Fe(1), Mo–P(2)). The fit resulted in insignificant changes in the 2-body parameters, and the agreement with crystallographic distances was within the sensitivity of the method. However, the R-value increased (from 1.46×10^{-6} to 1.68×10^{-6}), despite the substantial increase in the number of variables. The total number of variables at the Mo edge (43) compares with the number of independent parameters, N (as determined by $2(\Delta R)(\Delta k)/\pi$) of 33. However, even though the fit contains more variables than N, a lower R-value could not be found. In the case that a slightly lower R-value were found by introducing the 3-body signals, the meaningfulness of the results could be questioned. The inclusion of 3-body pathways, therefore, did not improve the quality of the fit. We conclude that 3-body MS signals are not important in this cluster. This is confirmed by inspection of the residual signals (Figures 7 and 8), which show no regular frequencies.

Fe K-Edge Results. These results, when compared with those

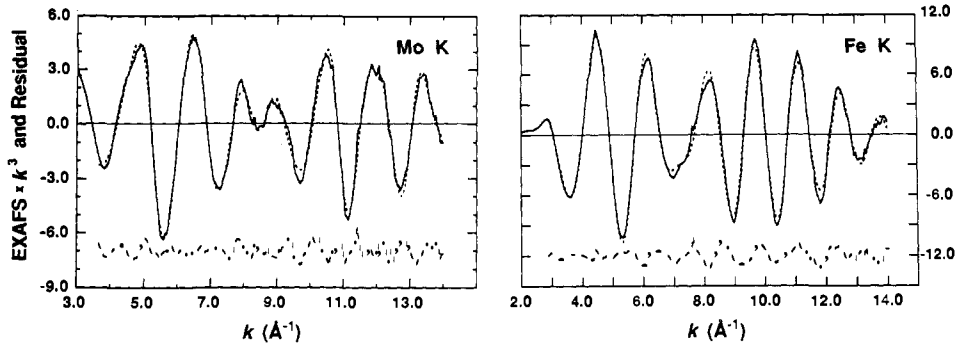

Figure 7. Comparison of experimental EXAFS data (—) for $MoFe_4S_6(PEt)_4Cl$ with best fits for Mo K (left) and Fe K (right) edges. The fit is shown as (···), and the residual between the experimental data and the fit, as (- - -). Details of fits and ranges are given in the Experimental Section and in the text. The residual is a very good indicator of the overall goodness-of-fit and can be monitored as incremental waves are added to the total EXAFS signal.

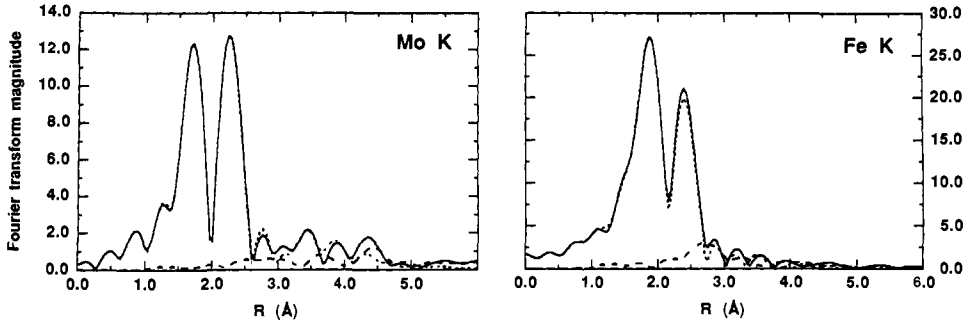

Figure 8. Comparison of Fourier transforms of the experimental data (—) with that for the total theoretical EXAFS signal (···) for Mo K (left) and Fe K (right) edges. Also shown is the Fourier transform of the residual (- - -). The residual can be monitored to indicate when added waves make a significant contribution to specific frequencies in the EXAFS.

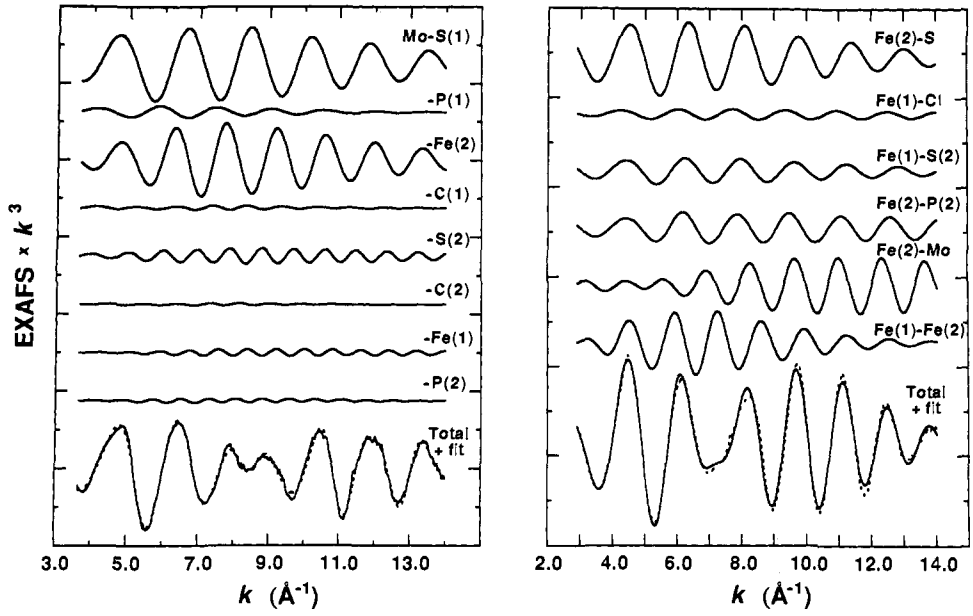

Figure 9. EXAFS signals for individual shells in the final fits for Mo K (left) and Fe K (right) data. The total signal is also shown and is compared with the experimental signal. (The abscissa scale is 8 (Mo) and 11 (Fe), indicated between two consecutive large marks.)

for the Mo K-edge analysis, show a slightly lower degree of accuracy for the distances below 3 Å (Table V), the average deviation being 0.024 Å. This is not surprising because four shells of atoms with similar backscattering amplitudes for two different types of Fe atoms fall in the range 2.24–2.31 Å. As a first approximation, contributions from the same type of backscattering atom at distances within 0.01 Å from either Fe(1) or Fe(2) were included as a single wave with the proper weights in the refinements (for example, Fe(2)–S values were consistently treated as an average). The total EXAFS signal was well accounted for by the six waves from the shells below 3 Å (Table V and Figures 7 and 8). Indeed, the Fourier transform shows only a small magnitude above 3 Å. Because the difference in distances for Fe(2)–S and Fe(1)–S were at the resolution limit of EXAFS over the range of available data, 5-shell fits were also performed with these two distances averaged. The results (not shown) revealed very similar metrical details and residual to the 6-shell results, with the Fe–S distance being determined to within 0.014 Å of the average crystallographic value.

Attempts to include contributions from shells beyond 3 Å did not give consistent results. There are an additional five shells between 3 and 4 Å and two more between 4 and 5 Å. The small

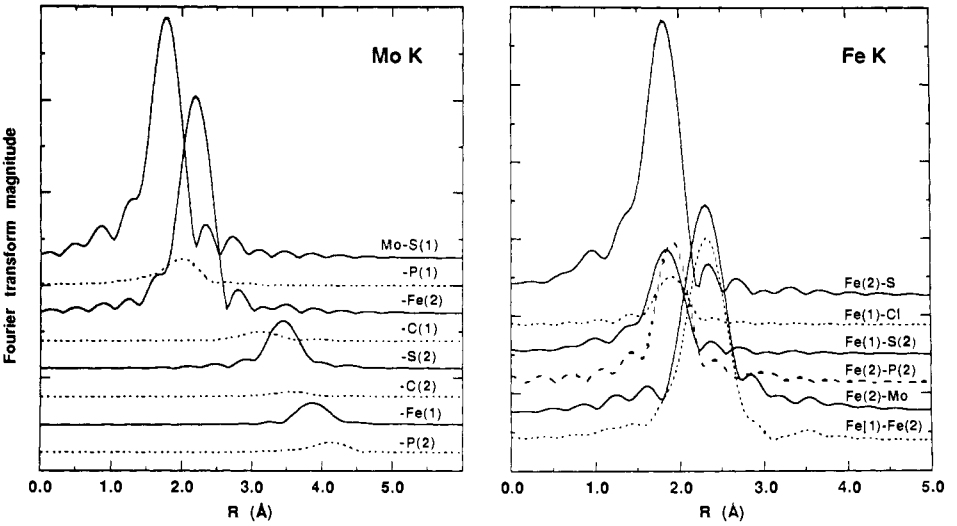

Figure 10. Fourier transforms of the EXAFS signals for the individual shells shown in Figure 9. This display is a useful way to determine which signals contribute in which regions of the Fourier transform. It is important to note that the width of the individual signals is broader than when they all sum in the overall transform. Thus, particularly for outer shells, it is not in general possible to filter specific shells in order to fit each separately. (The abscissa scale is 5 (Mo) and 4 (Fe), indicated between two consecutive large marks.)

Table V. Results from GNXAS Fits to the Fe K-edge Data of $MoFe_4S_6(PEt_3)_4Cl$[a]

bond	cryst dist (Å)	R[b] (Å)	DW[c] (Å^2)
Fe(2)–S	2.237	2.220	0.0053
Fe(1)–Cl	2.263	2.290	0.0020
Fe(1)–S(2)	2.283	2.250	0.0041
Fe(2)–P(2)	2.321	2.300	0.0013
Fe(2)–Mo	2.633	2.604	0.0021
Fe(1)–Fe(2)	2.709	2.695	0.0103
R-value[d]	4.55×10^{-8}		

[a] The total number of points in the fitting range k = 2.9–14.0 Å^{-1} was 243. (See text for discussion of errors.) [b] R = interatomic distance. [c] DW = Debye–Waller factor. [d] Least-squares residual: see text.

amplitude in the Fourier transform beyond 3 Å (Figure 8) results from a number of contributing signals, none of which could be uniquely identified with any given single shell in a statistically meaningful fashion. Further, 3-body signals were again very small (as at the Mo K-edge) and also did not appear to make contributions that could be correlated with individual features in the Fourier transform at higher R. The fact that the higher frequencies of the Fe EXAFS signal are not as well modeled as for the Mo EXAFS is also clearly seen by comparing their EXAFS residual signals (Figure 7). At this level of refinement, one can thus conclude that in this cluster it is not possible to detect reliably the long Fe–Mo interaction from the Fe K-edge EXAFS, in contrast to the Mo K-edge results. This limitation in the K-edge analysis is partially due to the existence of two different Fe sites in the structure.

Reliability of Parameter Determinations. The statistical error in the parameters estimated by the least-squares fitting procedure is very small (typically, one in the third/fourth significant decimal place, depending on the noise level of the experimental data). Error estimates can be made on the basis of how much a given variable must change to produce a given increase in the R-value within the variance of the experimental data. However, due to statistical correlation between different parameters of the fit, only a multidimensional contour plot of R in parameter space would provide the corresponding error. Systematic errors in the experimental data collection and the uncertainty in the theoretical signal give rise to systematic errors that can be much larger than the statistical ones. When a large set of fitting parameters is used, the best indication of these errors is the variance with known experimental results, as in the cluster EXAFS discussed here. From the comparison with crystallographic results, we conclude that, with this analysis method applied to relatively compact molecules, given good experimental data over a reasonable k-range, errors in distance determinations range from 0.01 to 0.02 Å for distances within 3 Å from the photoabsorber, to 0.03 Å for distances up to 4 Å, and to 0.05 Å for further shells. These levels of accuracy arise because the theory is quite reliable in reproducing the phase of the experimental signal, as confirmed by previous applications.[27,32,34–36] The amplitudes of the signals can be determined with slightly less accuracy. In fact, because amplitudes are affected in the fits by several variables which can be strongly correlated (S_o^2, E_r, molecular vibrations) and are not as well known theoretically, the best one can do to assess the errors in the determination of these parameters is to monitor their range of variation within reasonably good fits. This is especially true for DW factors where errors up to 100% are possible. The best strategy would be to use in addition theoretical or experimental values to limit the range of parameter variation, as done in the present study for the parameters S_o^2, Γ_c, and E_r. A future improvement should be to implement a valid approximation to molecular vibrations in order to provide reasonable limits for DW factors.

Summary and Conclusions. The following are the principal results and conclusions of this investigation:

(1) A new cluster self-assembly system in THF has been devised which affords the uncharged clusters $MFe_4S_6(PEt_3)_4Cl$ (M = V, Mo), identified by ^1H NMR, mass spectrometry, and X-ray diffraction.

(2) The isostructural compounds $MFe_4S_6(PEt_3)_4Cl$ present a new type of cluster architecture, wherein a cuboidal Fe_4S_3 fragment is bridged by three μ_2-S atoms to a $MPEt_3$ unit. The trigonal pyramidal coordination units FeS_3P and MS_3P are infrequently encountered and unprecedented, respectively. The cuboidal fragment has been previously observed only in Roussin's black anion $[Fe_4S_3(NO)_7]^-$ [55] and $Fe_4S_3(NO)_4(PPh_3)_3$,[56] in which the oxidation states are lower and metal–metal bonding is enhanced compared to the present clusters.

(3) Of the 17 core atoms (including Y) in the KR cofactor model **6** (Figure 1), *the clusters $MFe_4S_6(PEt_3)_4Cl$ present 10 atoms ($Fe_4S_3(\mu_2\text{-}S)_3$) with the analogous core bond connectivity and spatial disposition.* The trigonal pyramidal coordination at Fe(2,2′,2″) departs from the trigonal planar coordination at bridged Fe sites in the cofactor, a stereochemistry otherwise

(55) (a) Chu, C. T.-W.; Dahl, L. F. *Inorg. Chem.* **1977**, *16*, 3245. (b) Glidewell, C.; Lambert, R. J.; Harman, M. E.; Hursthouse, M. B. *J. Chem. Soc., Dalton Trans.* **1990**, 2685.

(56) Scott, M. J.; Holm, R. H. *Angew. Chem., Int. Ed. Engl.* **1993**, *32*, 564.

observed only in sterically congested $Fe_2(\mu_2\text{-}SR)_4$ (R = 2,4,6-tBu$_3$C$_6$H$_2$).[57] These clusters currently provide the closest structural approach to the cofactor cluster core.

(4) The GNXAS approach, which uses theoretical parameters to model the EXAFS signal, provides an accurate means of determining metrical details for neighboring atoms within about 3 Å of the absorber for cuboidal cluster systems. The results are comparable to or better than can be achieved with empirical phases and amplitudes, without dependence on obtaining suitable models from which to extract parameters. The spline-minimization protocol eliminates the tedious procedure of manual spline-background removal and results in spectra with slight residual low-frequency components.

(5) Accurate calculation of contributions to the total EXAFS signal has provided the opportunity to evaluate the importance of longer-distance contributions and to determine if they could be extracted reliably. Multiple scattering signals were calculated but were not found to be significant for this particular cuboidal cluster, a likely outcome for other clusters with internal bond angles significantly below 130°. It is clear that longer-distance (>4 Å) metal–metal interactions can be reliably detected under certain circumstances, as observed in the Mo EXAFS analysis. However, from the point of view of the Fe absorbers in the same cluster, longer distances cannot be reliably determined, probably due to the two different types of Fe sites.

(6) A comparison of the Mo EXAFS analysis for $MoFe_4S_6(PEt_3)_4Cl$ with that previously published for the FeMo-cofactor reveals interesting differences that derive from the presence of a distinct third shell of scatterers (low-Z) present in FeMo-cofactor, which give rise to six- rather than four-coordinate Mo as in the present cluster. The local Mo environment determined originally by EXAFS[14] has now been verified by the KR model. However, inspection of the FeMo-cofactor Fourier transforms of the Mo K-edge data[14b] reveals no clear evidence for longer-distance (>3 Å) ordered shells from the Mo atom. This observation is not surprising in view of the results presented herein, given the higher noise level of the published FeMo-cofactor data and the KR model in which the Mo to longer distance Fe shell across the cluster is around 5 Å. While EXAFS can clearly detect longer distances in such structures in some circumstances, due caution must be exercised.

(57) Power, P. P.; Shoner, S. C. *Angew. Chem., Int. Ed. Engl.* **1991**, *30*, 330.

Acknowledgment. This research was supported by NSF Grants CHE 89-03283 and 92-08387 and by NIH Grant 28856 at Harvard University and by NSF Grant CHE 91-21576 and NIH Grant RR-01209 at Stanford University. X-ray diffraction equipment was obtained by NIH Grant 1 S10 RR 02247. X-ray absorption data were collected at SSRL, which is supported by the U.S. Department of Energy, Office of Basic Energy Sciences, Divisions of Materials and Chemical Sciences. SSRL is also supported by the National Institutes of Health, Biomedical Research Technology Program, and by the U.S. Department of Energy, Office of Health and Environmental Research. We thank Professor E. Münck for a preprint of ref 13 and Professor D. Koningsberger for a preprint of ref 31 prior to publication.

Supplementary Material Available: Crystallographic data for the compounds in Table I, including tables of intensity collections, positional and thermal parameters, and interatomic distances and angles (7 pages); tables of calculated and observed structure factors (41 pages). Ordering information is given on any current masthead page.